Geochemistry, Geophysics, Geosystems®

AGU ADVANCING EARTH AND SPACE SCIENCE

RESEARCH ARTICLE
10.1029/2021GC010107

Special Section:
Slow Slip Phenomena and Plate Boundary Processes

# Frictional and Lithological Controls on Shallow Slow Slip at the Northern Hikurangi Margin

**Srisharan Shreedharan[1,2], Matt Ikari[3,4], Clay Wood[1], Demian Saffer[5,6], Laura Wallace[5,6,7], and Chris Marone[1,8]**

[1]Department of Geosciences, Pennsylvania State University, University Park, PA, USA, [2]Now at University of Texas Institute for Geophysics, Austin, TX, USA, [3]MARUM Center for Marine Environmental Sciences, University of Bremen, Bremen, Germany, [4]Faculty of Geosciences, University of Bremen, Bremen, Germany, [5]University of Texas Institute for Geophysics, University of Texas, Austin, TX, USA, [6]Department of Geological Sciences, University of Texas, Austin, TX, USA, [7]GNS Science, Lower Hutt, New Zealand, [8]Dipartimento di Scienze della Terra, La Sapienza Universitadi Roma, Rome, Italy

**Abstract** Slow slip events (SSEs) have been identified at subduction zones globally as an important link in the continuum between elastodynamic ruptures and stable creep. The northern Hikurangi margin is home to shallow SSEs which propagate to within 2 km of the seafloor and possibly to the trench, providing insights into the physical conditions conducive to SSE behavior. We report on a suite of friction experiments performed on protolith material entering the SSE source region at the Hikurangi margin, collected during the International Ocean Discovery Program Expedition 375. We performed velocity stepping and slide-hold-slide experiments over a range of fault slip rates, from plate rate (5 cm/yr or $1.6 \times 10^{-9}$ m/s) to ~1 mm/s ($10^{-3}$ m/s) and quantified the frictional velocity dependence and healing rates for a range of lithologies atdifferent stresses. The frictional velocity dependence ($a$-$b$) and critical slip distance DC increase with fault slip rate in our experiments. We observe atransition from velocity weakening to strengthening at slip rates of ~0.3 μm/s. This velocity dependence of DC could be due to a combination of dilatant strengthening and a widening of the active shear zone at higher slip rates. We document low healing rates in the clay-rich volcaniclastic conglomerates, which lie above the incoming plate basement at least locally, and relatively higher healing rates in the chalk lithology. Finally, our experimental constraints on healing rates in different input lithologies extrapolated to timescales of 1–10 years are consistent with the geodetically inferred low stress drops and healing rates characteristic of the Hikurangi SSEs.

**Key Points:**

- We quantify frictional stability and healing behavior of input material to the subduction plate interface at the northern Hikurangi margin
- Increasing frictional stability and critical slip distance with velocity may be key mechanisms responsible for shallow slow slip
- Velocity dependence of critical slip distance may be from a combination of dilatant strengthening and distributed slip at higher slip rates

**Supporting Information:**

Supporting Information may be found in the online version of this article.

**Correspondence to:**

S. Shreedharan,
srisharan@utexas.edu

**Citation:**

Shreedharan, S., Ikari, M., Wood, C., Saffer, D., Wallace, L., & Marone, C. (2022). Frictional and lithological controls on shallow slow slip at the northern Hikurangi margin. *Geochemistry, Geophysics, Geosystems*, *23*, e2021GC010107. https://doi.org/10.1029/2021GC010107

Received 19 AUG 2021
Accepted 22 JAN 2022



## 1. Introduction

Slow slip events (SSEs), lasting for days to months, have been widely recognized as an important part of the continuum bridging fast, elastodynamic ruptures and stable fault creep at plate boundaries globally (Bürgmann, 2018; Ide et al., 2007; Peng & Gomberg, 2010). These types of slip modes are particularly important because of the role they play in the seismic cycle and the accommodation of plate motion, and because of the clues they provide about plate interface rheology. In some cases, SSEs are thought to trigger ordinary fast earthquakes by loading adjacent fault patches (Kato et al., 2012; Meng et al., 2015). In other cases, SSEs have been triggered (Araki et al., 2017; Wallace et al., 2017) or arrested (Wallace et al., 2014) by nearby earthquakes. Thus, the precise role played by SSEs in the overall earthquake cycle is unclear. Moreover, many SSEs at convergent margins globally have been documented at the downdip limit of the seismogenic zone, that is, at depths of 30–40 km (Schwartz & Rokosky, 2007), which makes it impossible to directly sample and study the frictional behavior of the active SSE source rocks.

The northern Hikurangi margin, offshore New Zealand, is an important example of shallow and accessible SSEs. These faults host robustly documented, quasi-periodic shallow SSEs (Wallace, 2020) that rupture close to the trench (Wallace et al., 2016) and have recurrence intervals of 12–18 months. Additionally, the source region of these SSEs has hosted tsunami earthquakes which may have ruptured to the trench (Bell et al., 2014) and is hypothesized to have significant pore fluid overpressure (Bassett et al., 2014; Bell et al., 2010; Ellis et al., 2015). Thus, it is important to constrain the frictional behavior of the source material to better understand the rock properties and processes that govern fault slip behavior, and ultimately the future risk of earthquake and tsunami generation.

Numerous studies have been undertaken in the laboratory to constrain the frictional behavior of natural fault zones (e.g., Carpenter et al., 2011; Carpenter et al., 2016; Ikari et al., 2009; Ikari & Saffer, 2011; Ikari, Wallace, et al., 2020) and subduction inputs (e.g., Kurzawski et al., 2016; Rabinowitz et al., 2018). Specifically, of paramount importance are the frictional strength and the sliding stability of sheared faults. The latter quantity is usually defined within the framework of rate and state friction or RSF (Marone, 1998), which describes a set of constitutive equations motivated by laboratory experiments (Dieterich, 1978, 1979; Ruina, 1983). Broadly, laboratory observations of sliding friction can inform us about whether a fault will slide stably, resulting in aseismic creep, or unstably, giving rise to a range of slip modes including SSEs and fast dynamic earthquakes. Within this framework, SSEs arise naturally as a bridge between aseismic creep and elastodynamic ruptures based on an interaction between the fault zone elastic loading stiffness and a critical fault stiffness (Gu et al., 1984; Im et al., 2020; Leeman et al., 2016, 2018; Scuderi et al., 2017).

Recently, the International Ocean Discovery Program (IODP) Expeditions 372 and 375 sailed to the Hikurangi margin and sampled materials on the incoming Pacific Plate prior to subduction into the SSE region (Barnes et al., 2019). This provides an opportunity to sample and quantify the frictional behavior of materials likely playing an important role in hosting shallow SSEs. In particular, two distinct lithologies (chalks and phyllosilicate-rich volcaniclastic conglomerates) are abundant and likely represent a significant portion of the materials being subducted to the SSE source region based on tracing the seismic stratigraphy from the drill sites to the shallow subduction thrust (Barnes et al., 2020). Here, we present results from laboratory friction experiments designed to measure the frictional strength, sliding stability and healing behavior of these materials, at stresses and pore fluid pressures appropriate for conditions in the shallow SSE source area. We present results over a range of fault slip rates, from plate tectonic rates, that is, ~5 cm/yr (e.g., Ikari et al., 2015), to slip rates of 1 mm/s, which far exceed the peak slip rates of the shallow SSEs in the study region.

## 2. The Hikurangi SSEs and IODP Expeditions 372/375

The Hikurangi subduction margin accommodates westward subduction of the Pacific plate beneath the Australian plate (Figure 1a) at a rate of ~2–6 cm/yr, with convergence rates reducing along-strike from North to South (Wallace et al., 2004). A range of SSEs, with significant along-strike variations, have been documented in this region (Wallace, 2020 and refs. therein). In particular, the northern Hikurangi SSEs are shallower (depths <15 km), marked by shorter recurrence intervals (12–18 months) and durations (2–3 weeks; Wallace & Beavan, 2010), and have been documented to propagate very close to the trench (Wallace et al., 2016). In contrast, the deeper (25–50 km depth) SSEs at the southern Hikurangi margin are marked by longer durations (3–24 months) and recurrence intervals of 4–5 years (Bartlow et al., 2014; Wallace & Beavan, 2010). Furthermore, the source region of the northern Hikurangi shallow SSEs is interpreted to be lithologically and geometrically heterogeneous (Barnes et al., 2020). For example, reflection seismic surveys (Figure 1b) show that the SSE source region is broadly coincident with high reflectivity zones (Bell et al., 2010) inferred to be regions of high pore fluid pressure and seamount subduction (Barker et al., 2018; Bell et al., 2014; Todd et al., 2018). Thus, these heterogeneities have been thought to play an important role in the nucleation of shallow SSEs and the interplay between SSEs and tsunami earthquakes. However, the physical processes surrounding the origins of these diverse SSE behaviors in this region remain poorly resolved, in part, because it is not easy to directly sample the source rocks.

IODP Expeditions 372 and 375, which sailed in late 2017 and early 2018, drilled at four sites to sample the upper plate, a splay fault (near the deformation front), and the sedimentary sequence on the incoming plate (Figure 1b) at the northern Hikurangi margin, offshore Gisborne, New Zealand (Wallace et al., 2019). Based on reflection seismic surveys and seismic correlations with core and logging data, key lithologies involved in the source region of the shallow SSEs have been identified as lying below 510 m below seafloor (mbsf) at site U1520 (Barnes et al., 2020). Specifically, marls and chalk were found at 510–849 mbsf, and the lower portion of the sediment package (below 849 mbsf) consists of a volcaniclastic facies (Figure 2). The latter material contains basalt clasts, a clay-rich (primarily saponite) altered matrix and zeolite cementation and, for a few tens of meters, carbonate-rich cementation (Figure 2; Barnes et al., 2019; Underwood, 2020). Data from seismic reflection surveys (e.g., Bell et al., 2014) and regional drilling (Barnes et al., 2020) point to a plate interface which is likely patchy due to the heterogeneous incoming protolith containing regionally variable thicknesses of the carbonate and volcaniclastic sediments.

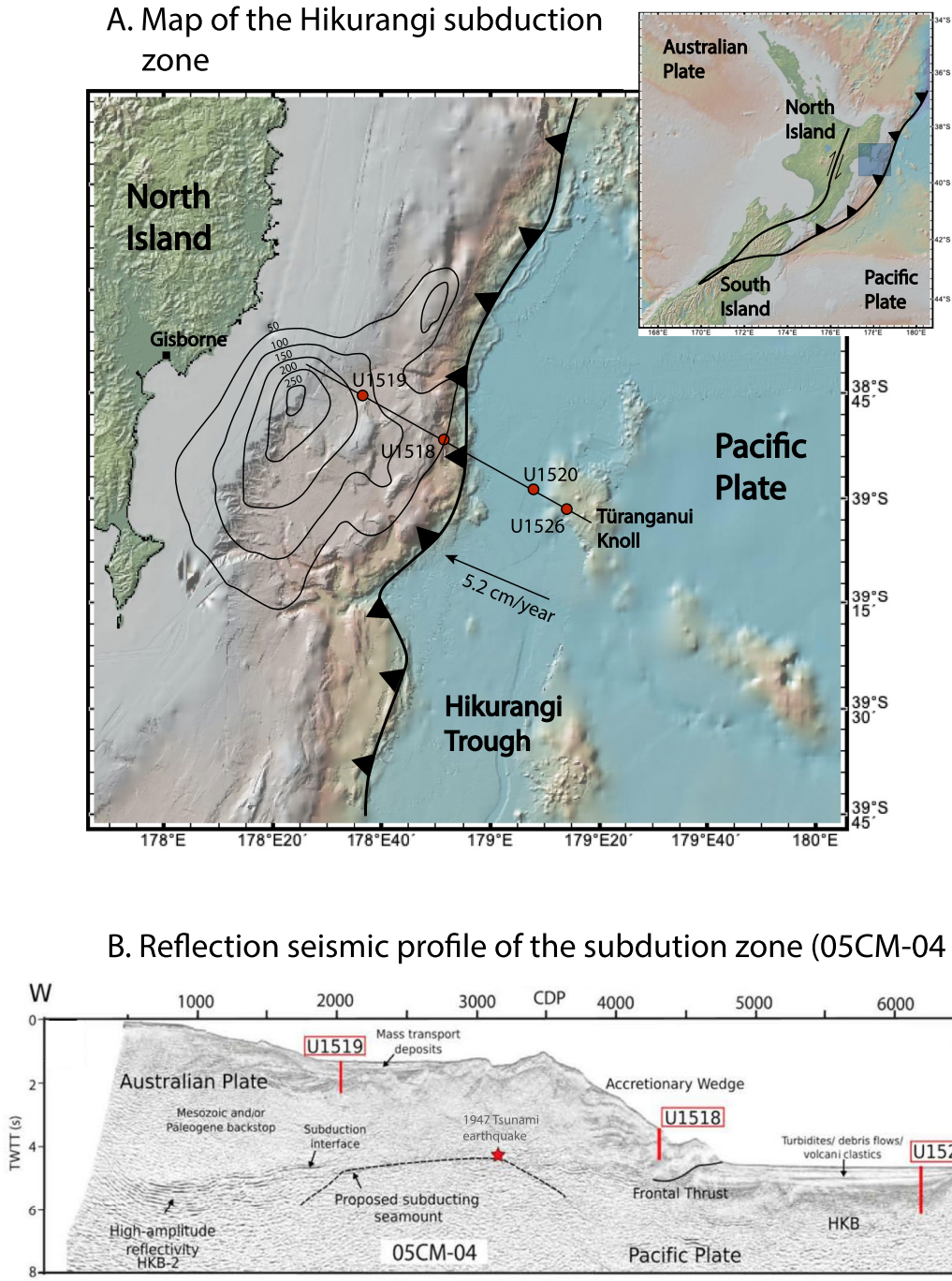


**Figure 1.** (a) Map of New Zealand showing the Hikurangi Trough and interface between the subducting Pacific and overlying Australian plates. The black line and red dots show the location of seismic line 05CM-04 and IODP Expedition 372/375 drill-sites respectively. Black curves on the upper plate show 50 mm slip contours from the 2014 slow slip events (SSE) (Wallace et al., 2016). (b) Two-way travel time versus common depth point for processed seismic line 05CM-04 showing the locations of various drill sites targeted during International Ocean Discovery ProgramExpedition 375, the hypocenter of the 1947 Tsunami earthquake (red star) and a proposed subducting seamount at the subduction plate interface (After Gray et al., 2019).

While clay- (and particularly smectite) rich sediments have been documented as being weak with a tendency for velocity-strengthening frictional behavior (e.g., Ikari et al., 2009; Ikari & Saffer, 2011; Saffer & Marone, 2003; Ujiie et al., 2013), carbonate-rich sediments are usually significantly stronger and can exhibit velocity weakening behavior especially at elevated temperatures (Ikari et al., 2013; Kurzawski et al., 2016; Tesei et al., 2014). Field, modeling and experimental studies (e.g., Ando et al., 2010; Boulton et al., 2019; Nakata et al., 2011; Skarbek

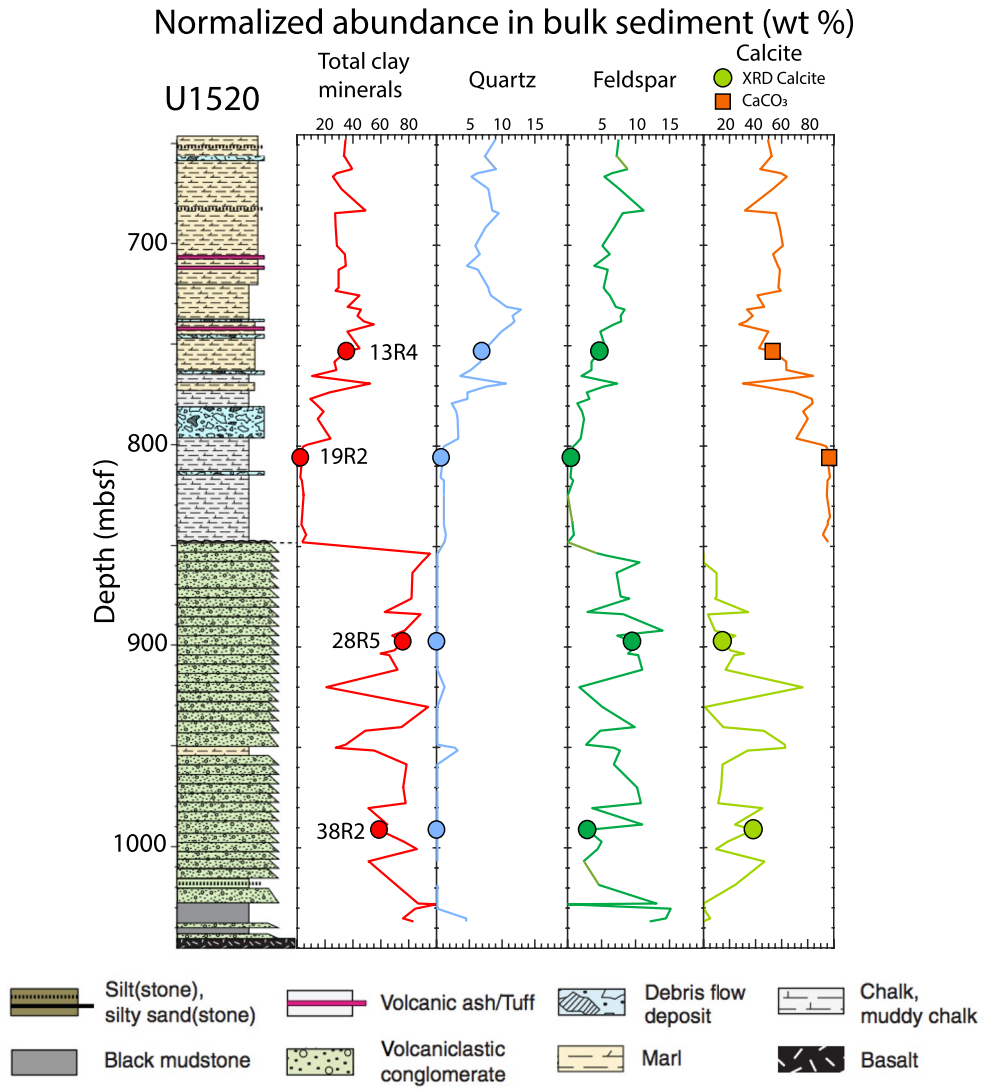


**Figure 2.** Depth section of various lithostratigraphic units at site U1520 and bulk sediment mineralogical composition of the samples used in this study.

et al., 2012) have reported that geologic and lithological heterogeneities, that is, mixtures of velocity weakening and strengthening sediments along plate interfaces may offer one explanation for the generation of SSEs. Previous studies reporting the frictional behavior of inputs to the Hikurangi margin (Boulton et al., 2019; Ikari, Wallace, et al., 2020; Rabinowitz et al., 2018) focused on shallower sediments (200–450 mbsf) farther from the trench, from Ocean Drilling Program (ODP) Site 1124. Here, we present results from friction experiments conducted on a larger range of lithologies, and over a wider range of shearing rates and pore pressure conditions.

## 3. Methods

### 3.1. Double-Direct Shear Experiments (0.3–1,000 μm/s)

Biaxial experiments were conducted in a true-triaxial pressure vessel in a double direct-shear (DDS) configuration in the Penn State Rock and Sediment Mechanics Laboratory (e.g., Samuelson et al., 2009). In this configuration, servo-controlled horizontal and vertical pistons directly apply normal ($\sigma$) and shear stresses ($\tau$), respectively, to two gouge layers sandwiched between three steel blocks (Figure 3a). Confining ($P_c$) and pore fluid pressures (inflow—$P_{pA}$ and outflow—$P_{pB}$) are independently servo-controlled via pressure intensifiers. Normal stress is applied on the gouge layers (30 $cm^2$ nominal contact area) as a load boundary condition. Shear is applied on the

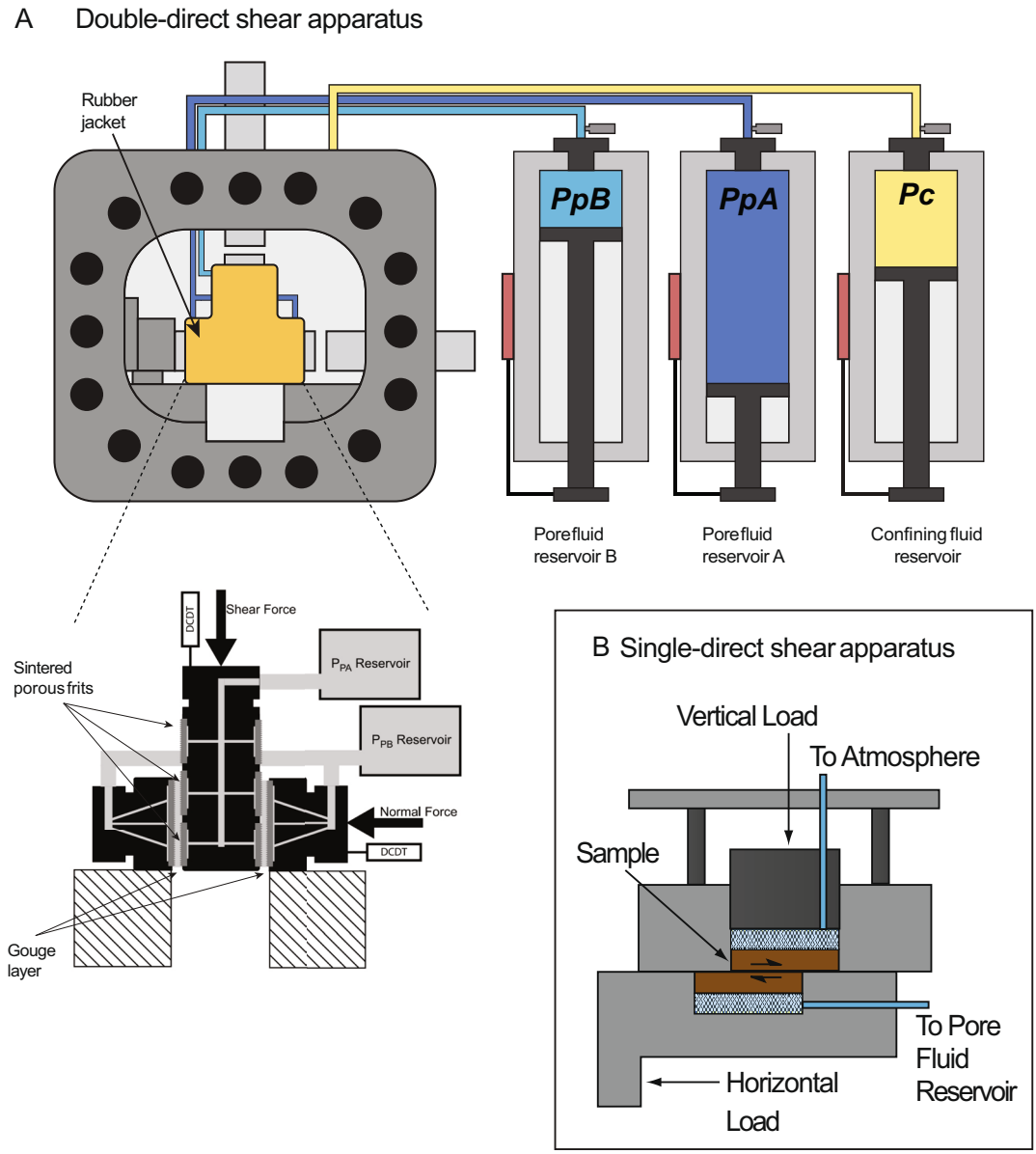


**Figure 3.** Schematic of experimental apparatuses used in this study. (a) Samples in the biaxial apparatus are sheared in a double direct-shear configuration in a true-triaxial stress state with independent inlet (PpA) and outlet (PpB) pore fluid reservoirs. Normal and shear stresses are supplied by a horizontal and vertical piston respectively. The sample rests in a pressure vessel and is separated from the surrounding confining fluid (oil) by a rubber jacket. Inset to (a) shows the powdered sample (gouge) sandwiched between three grooved steel blocks with internal plumbing for pore fluid flow. (b) Samples in the Giesa apparatus are saturated and sheared in a single direct-shear configuration with a fixed top plate and a moving base plate. A vertical piston supplies the normal load and a horizontal piston supplies the shear load.

longer central forcing block through a prescribed loading/shearing rate, thus deforming the sandwiched gouge layers. Grooves in sintered frits ensure that deformation occurs within the gouge layers rather than localizing at the steel-gouge interface (Figure 3a) and provides spatially uniform fluid access to the fault zone. A confining pressure (oil-based) is applied to achieve a true triaxial stress state. Rubber jackets surrounding the DDS assembly ensure that the pore fluids in the sample remain isolated from the oil-based confining pressure. In experiments where pore pressure is applied, the gouge layers are initially saturated by applying a constant pressure to the pore fluid (de-ionized water) at the inflow end, and the outflow end is connected to a vacuum pump. This ensures that the pore spaces are completely filled with the pore fluid. In our experiments, a constant pore pressure was applied on both the inflow and outflow sides during shear, keeping the sample under a drained boundary condition. While

**Table 1**
*List of Experiments and Boundary Conditions*

| Experiment no. | Sample name | Apparatus | Effective normal stress, $\sigma_{eff}$ (MPa) | Pore pressure, $P$ | Saturation state | Shear velocities (μm/s) |
|---|---|---|---|---|---|---|
| p5200 | U1520C13R4 | DDS | 25 | 0 | 100% RH | 1–1000 |
| p5391 | U1520C38R5 | DDS | 25 | 5 | Saturated | 0.3–300 |
| p5392 | U1520C28R5 | DDS | 25 | 5 | Saturated | 0.3–300 |
| p5393 | U1520C19R2 | DDS | 25 | 5 | Saturated | 0.3–300 |
| p5419 | U1520C28R5 | DDS | 25 | 0, 17 | Saturated | 0.3–1000 |
| p5454 | U1520C28R5 | DDS | 25 | 0 | 100% RH | 0.3–1000 |
| B875gds | U1520C38R2 | SDS | 25 | 0 | Saturated | 0.00165–1.65 |
| B984gds | U1520C19R1 | SDS | 25 | 0 | Saturated | 0.0016–1.65 |
| B1026gds | U1520C28R5 | SDS | 25 | 0 | Dry | 0.0016–1.65 |
| B1060gds | U1520C13R3 | SDS | 25 | 0 | Saturated | 0.0016–1.65 |
| B1067gds | U1520C28R5 | SDS | 25 | 0 | Saturated | 0.0016–1.65 |

a temporarily undrained condition is possible internally in the gouge layers, past studies (Ikari et al., 2009) have demonstrated that significant pore pressure transients do not develop in our configuration. Previous studies have quantified that the rubber jackets have negligible strength (Samuelson et al., 2009).

Normal and shear loads are measured using strain gauge load cells with a resolution of 0.1 kN. Fault normal and shear displacements are measured using direct-current linear variable differential transformers (DC-LVDTs). Confining pressure and associated volumetric changes are measured using a pressure transducer and a DC-LVDT affixed to the $P_c$ intensifier. In the case of pore pressures, the pressure transducers are located close to the sample in order to minimize sensing volume and thus measure any small variations, whereas the displacement transducers (for measuring volumetric changes) are fixed to the $P_{pA}$ and $P_{pB}$ intensifiers. All pressure transducers have a measurement resolution of 7 kPa. Mechanical data are acquired continuously at 10 kHz and averaged to 100–1,000 Hz in real-time for storage. All experiments were conducted at an effective normal stress ($\sigma_{eff}$) of 25 MPa, over a range of pore pressures and slip rates, from sub-slow slip rates of 0.3 μm/s (~1–3 cm/day at the northern Hikurangi margin) to 1,000 μm/s Table 1 contains the list of experiments and associated boundary conditions.

Input material sampled at four depth intervals (Figure 2) from Site U1520 were reconstituted and dried in an oven in vacuum at 40°C for 48 hr. Subsequently, the dry rocks were crushed, ground and sieved to a particle size of <125 μm. Note that an entire interval of core (~5 cm long) co-located with the samples used for mineralogical analyses (Figure 2) was reconstituted and homogenized to ensure representative sampling and prevent fractionation of mineral species. Gouge layers were constructed with a measured mass of material to ensure reproducibility and to a thickness of 5 mm width in a levelling jig (dry and under atmospheric pressure conditions). Layer thickness was measured prior to load application and at multiple points after the normal stress was applied, in order to calculate shear strains. Deionized water (DI) was used to saturate the samples since the drying process precipitates dissolved salts from the seawater into the sample. Thus, during saturation, we expect the salts to dissolve into the DI water bringing the brine concentration and chemistry back to levels that may closely resemble in-situ brine concentration.

Each experiment in the biaxial configuration consisted of a similar loading and shearing protocol. We conducted 1–2 unload/reload cycles during the first 5 mm of shear (Figure 4) to accelerate the development of a steady-state frictional behavior (Frye & Marone, 2002; Mair & Marone, 1999; Saffer et al., 2001). We followed this with a sequence of velocity steps (0.3–1,000 μm/s) with ~0.5 mm of slip per velocity and slide-hold-slide experiments (1–3,000 s hold times) over a displacement range of up to 25 mm (Figure 4a).

### 3.2. Single-Direct Shear (SDS) Experiments ($10^{-13}$–1 μm/s)

Low-velocity experiments were performed in a Giesa RS5 direct shear apparatus (Figure 3b) to explore the frictional behavior of the U1520 input material over a range of slip rates from plate-rate (1.6 nm/s, or 5 cm/yr)

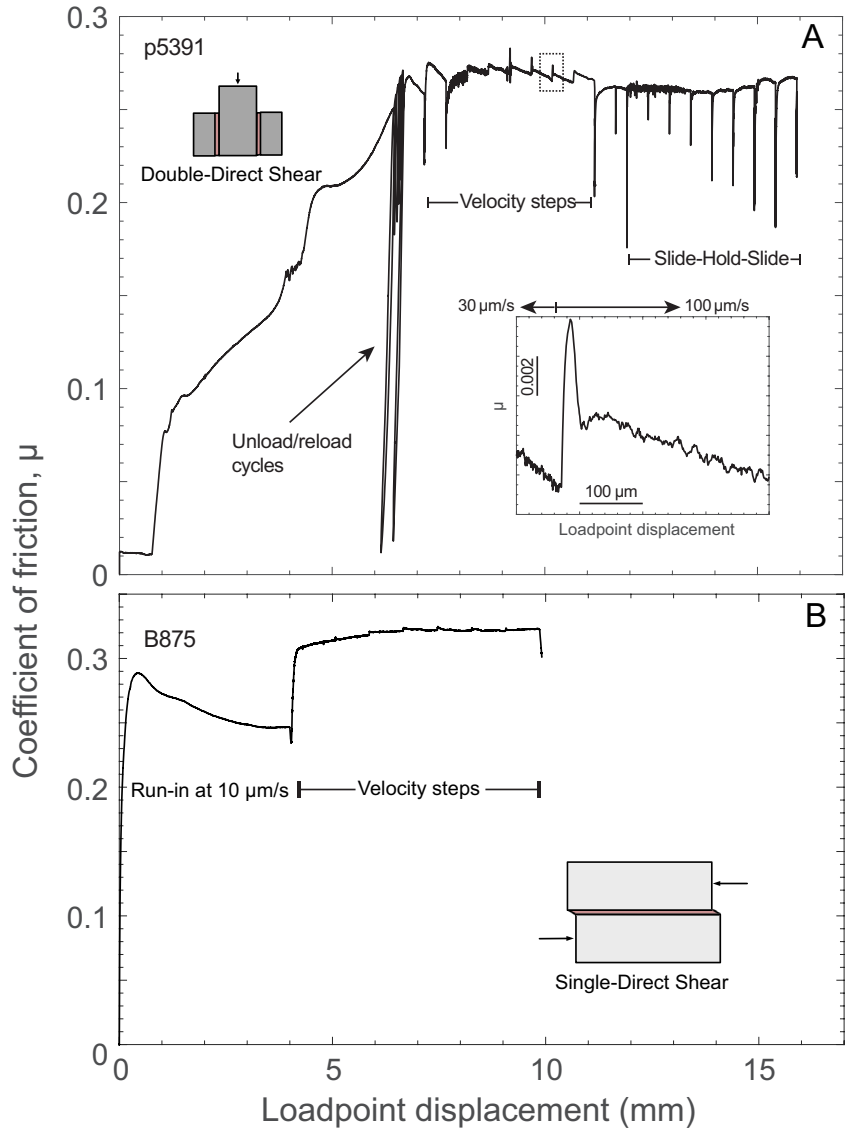


**Figure 4.** A plot of friction versus loadpoint displacement for a representative experimental run in (a) Double-direct shear and (b) Single-direct shear configurations shows various aspects of each experiment including unload/reload cycles to constrain initial loading stiffness, velocity step sequences and slide-hold-slide sequences. Inset to (a) shows the evolution of friction for a velocity step from 30 to 100 μm/s.

to slow-slip rates (0.5 μm/s, or 4.3 cm/day). In this experimental configuration, disaggregated gouge was mixed with DI water to create a water-saturated paste and placed in a sample cell (Ikari et al., 2015). The samples were sandwiched between porous steel frits at room temperature and DI water saturated conditions. The normal stress was applied vertically by vertical ram acting on a fixed top plate and the shear/loading rate was imposed by translating the base plate (Figure 3b). This forced shear to localize along a narrow zone (up to ~100s of μm thickness) as the two halves of the sample slide past each-other. Shear displacements were measured at two locations—one referenced to a horizontal, shear load cell (with resolution 0.3 kPa) measured the imposed shear displacement (or load point displacement) and another referenced to the sample measured the slip accommodated by the sample itself. The sample freely communicates with the pore fluid reservoir, and is allowed to drain to the atmosphere in order to dissipate local pore pressure development. On application of the normal load (25 MPa), the sample was allowed to consolidate and drain to the atmosphere for at least ~18 hr, until a steady state sample thickness was achieved, prior to shear. Thus, by the nature of the experimental design, pore pressures were not measured, but the sample was assumed to be under drained, zero pore pressure conditions before shearing. Additionally,

because the strain rates in this configuration are extremely low, we do not expect significant excess pore pressures to develop locally in the sample.

Samples were sheared at a run-in velocity of 10 μm/s for ~4–5 mm until a steady-state friction coefficient was achieved. Subsequently, velocity step experiments were conducted over the range of 1.6 nm/s to 0.5 μm/s with ~1 mm of slip per velocity (Figure 4b).

### 3.3. Estimation of RSF Parameters

In all experiments, the coefficient of friction (or simply referred to as friction), $\mu$, is defined as the ratio of shear stress, $\tau$, to effective normal stress, $\sigma_{eff}$.

$$\mu = \frac{\tau}{\sigma^{\text{eff}}} \tag{1}$$

In Equation 1, $\sigma_{eff}$ is the combined effect of the applied normal stress, $\sigma_N$, the net confining pressure acting normal to the gouge layers, and the applied pore pressure, $P_p$, and can be represented as

$$\sigma_{\text{eff}} = (\sigma_N + 0.629 P_C) - P_P \tag{2}$$

Within the framework of RSF, the velocity dependence of friction can be described as follows:

$$\mu = \mu_0 + a \ln\left(\frac{V}{V_0}\right) + b_1 \ln\left(\frac{\theta_1}{\theta_{1,0}}\right) + b_2 \ln\left(\frac{\theta_2}{\theta_{2,0}}\right) \tag{3}$$

In Equation 3, $a$, $b_1$, and $b_2$ are empirically determined constants, $V$ is the fault slip rate, $\theta_1$ and $\theta_2$ are state variables and the subscript "0" represents these quantities at an arbitrary reference state. Normally, most velocity step experiments can be well-described by a single state variable, although some velocity steps which are poorly fit by a 1-state variable RSF equation are better fit by a two-state variable law (Marone, 1998; See Supporting Information S1) as described in Equation 3. The RSF constants $a$ and $b$ are usually taken to represent some thermally activated contact-scale Arrhenius-type process and a measure of the real area of asperity contact, respectively (Ikari et al., 2016; Scholz, 2019). The state variable, $\theta$, represents contact age or contact lifetime (i.e., rapidly sliding contacts have a smaller contact age than slowly deforming contacts) and is represented as the ratio of a critical slip distance, $D_c$, and the asperity/contact sliding velocity. The evolution of frictional state (in a one- or two-state variable case) in response to a perturbation is usually expressed in one of two functional forms as the time-dependent Dieterich/aging law (Dieterich, 1979) or the slip-dependent Ruina/slip law (Ruina, 1983).

$$\frac{d\theta}{dt} = 1 - \frac{V\theta}{D_c} \text{ (Aging Law)} \tag{4}$$

$$\frac{d\theta}{dt} = -\frac{V\theta}{D_c} \ln\left(\frac{V\theta}{D_c}\right) \text{ (Slip Law)} \tag{5}$$

We invert for the RSF parameters $a$, $b$, and $D_c$ using a least squares procedure in RSFit3000 (Skarbek & Savage, 2019) by simultaneously solving Equation 3, and either Equation 4 or 5 with a 1D elastic coupling equation described by

$$\frac{d\mu}{dt} = k\,(V_{lp} V) \tag{6}$$

In Equation 6, $k$ represents the loading stiffness of the experiment and $V_{lp}$ is the imposed shear rate.

We only report values of the RSF parameters from those velocity steps where the coefficient of determination ($R^2$) is higher than 0.9. Thus, these inversions represent excellent fits to our experimental data. We performed RSF inversions using both the aging and slip laws for all velocity steps. However, we only report the RSF parameters from the aging law fits here since the slip law inversion consistently failed or had standard deviations greater than the mean value of the RSF parameter for higher sliding velocities. We quantify fault restrengthening by measuring frictional healing over different hold times during which the load point is held stationary (e.g., Yasuhara et al., 2005). We define frictional healing (Beeler et al., 1994; Dieterich, 1972) as the difference between

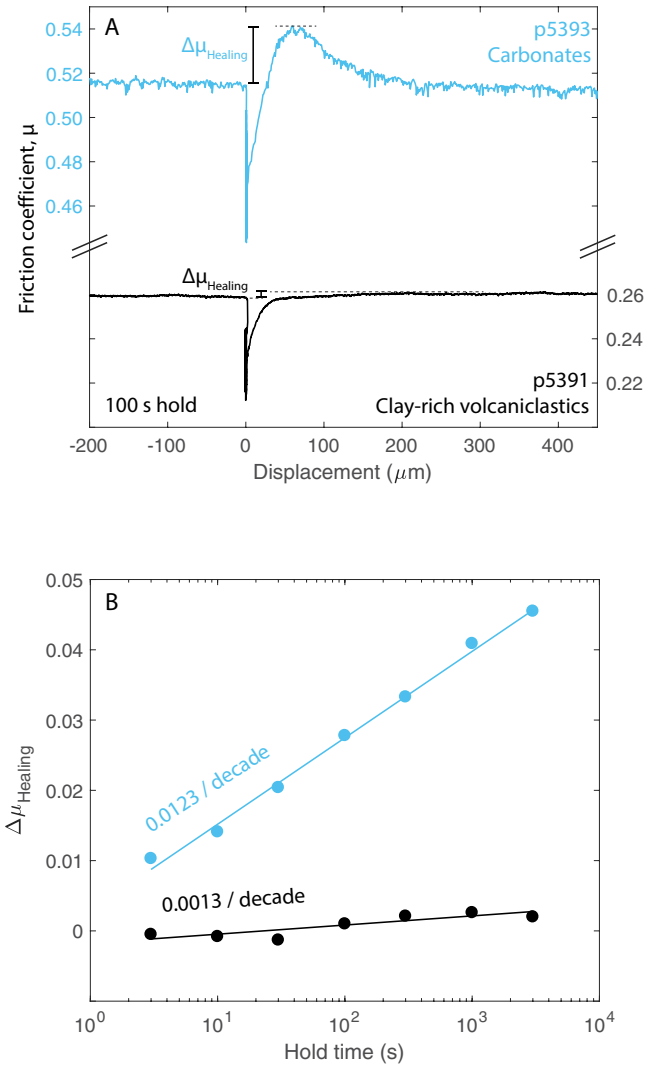


**Figure 5.** Friction evolution during slide-hold-slide experiments (a) and healing rates (b) in volcaniclastic conglomerates (black) and carbonates (blue) shows the significantly higher frictional healing rates in carbonates as compared to the clay-rich volcaniclastics.

peak friction upon re-shear after a hold and the previous steady state friction ($\Delta\mu_{Healing}$; Figure 5a) and the healing rate, β, as the frictional healing per decade hold time (Figure 5b).

## 4. Results

### 4.1. Slide-Hold-Slide Experiments

We observe distinctly different healing behaviors for the smectite-rich volcaniclastic facies and the chalks (Figure 5). The volcaniclastic conglomerates exhibit no post-hold peak friction upon reshear and near-zero healing rates (β = 0.0013/decade), similar to low values of frictional healing for clay-rich fault rocks and synthetic gouges reported in previous studies (e.g., Carpenter et al., 2012; Carpenter et al., 2016; Saffer & Marone, 2003; Tesei et al., 2012) for talc and montmorillonite gouges. On the other hand, the chalk lithology exhibits higher frictional healing, with healing rates (β = 0.0123/decade; Tesei et al., 2014).

### 4.2. Velocity Stepping Experiments

Velocity stepping experiments allow us to define the rate-dependent friction parameter (a-b) and invert individually for the RSF parameters $a$, $b$ and $D_c$ (Figure 6). In the case of two-state variable fits to velocity steps, we report the RSF parameter $b$ as the sum of $b_1$ and $b_2$. Our results indicate that "$a$" exhibits a modest velocity dependence (Figure 6a) while "$b$" is relatively insensitive to sliding velocity (Figure 6b). Over a range of velocities spanning plate rates (0.0016 μm/s) to faster-than-slow-slip rates (~300 μm/s), we document a bimodal behavior of friction velocity dependence (Figure 6c). Specifically, the volcaniclastic conglomerates are largely velocity neutral or slightly velocity weakening over slip rates ranging from plate-rate to slow slip rates at the northern Hikurangi margin. At ~0.3 μm/s, this behavior transitions to a steady increase in the frictional stability parameter (a-b) with fault slip rate for both the carbonates and the volcaniclastic facies. This form of a second-order rate dependence of friction, that is, the rate dependence of frictional rate dependence has previously been documented in experiments conducted on a range of material including synthetic mixtures of clay minerals and quartz (Ikari et al., 2009; Kaproth & Marone, 2014; Saffer et al., 2001), and on natural samples from various tectonic settings (Rabinowitz et al., 2018; Saito et al., 2013) including those that host shallow SSEs (Saffer & Wallace, 2015).

The critical slip distance, $D_c$, shows a slip rate dependence varying as $\sim V^n$, with $n$ = 0.3–1, over the range of velocities explored (Figure 6d). However, $D_c$ is apparently velocity invariant for the velocity steps conducted in the single-direct shear apparatus (circles in Figure 6d and Supplementary Figure S2). Since we model some of our velocity steps with a single-state variable formulation and others with the two-state variable equation, the $D_c$ reported in Figure 6d represents the (larger) $D_{c2}$ for velocity steps where the two- state variable RSF framework was used to invert our experimental data. We do so because we are interested in determining the variation of the total slip displacement required to reach a steady-state friction due to perturbations in the driving velocity, and $D_{c2}$ is a better representative of this quantity. Few studies have documented a robust velocity dependence of $D_c$. However, our results closely match two cases where this velocity dependence has been documented in quartz gouge (Mair & Marone, 1999) and natural sediment (Ikari, Carpenter, et al., 2020) from the Waikukupa Thrust in southern New Zealand (Figure 6d). Our results demonstrating the velocity dependence of RSF parameters are consistent over a variety of hydration states (humid/saturated) and pore pressures (Figures 6c and 6d).

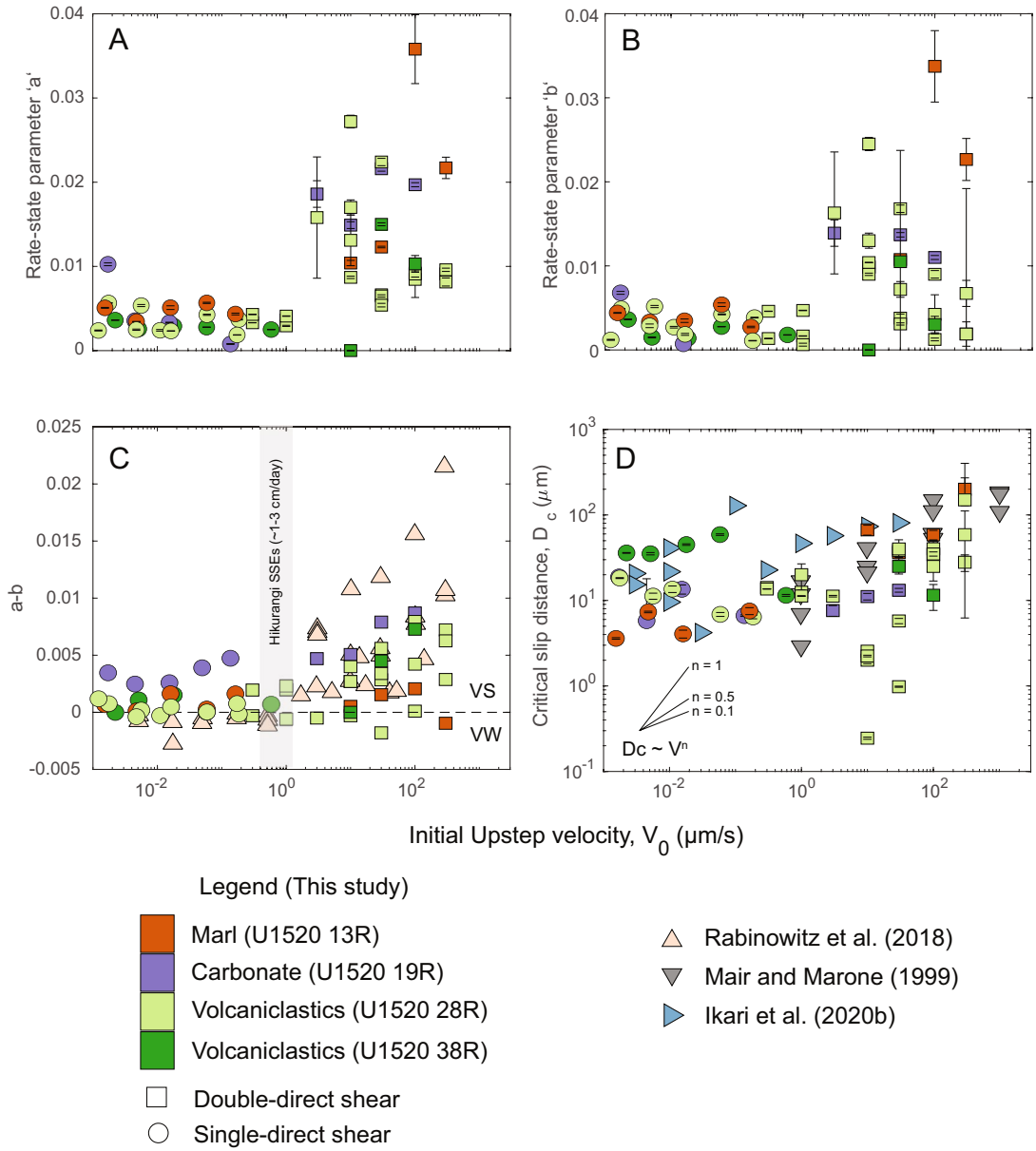


**Figure 6.** Evolution of rate-state friction (RSF) parameters with fault initial velocity prior to an upstep for (a) RSF parameter "*a*" (b) RSF parameter "*b*" (c) the difference (*a*-*b*) which marks the fault frictional stability as velocity weakening or velocity strengthening and (d) the critical slip distance, $D_c$. Different colors represent different material/samples and the symbols represent double direct-shear (square) and single-direct shear (circle) apparatuses.

## 5. Discussion

Here we discuss the implications of the velocity dependence of the rate-state frictional parameters (*a, b* and $D_c$) in our experiments and those of others (Ikari, Carpenter, et al., 2020; Mair & Marone, 1999) for a range of different natural and synthetic fault gouges. A necessary criterion for the emergence of any kind of unstable slip in numerical simulations (Gu et al., 1984; Im et al., 2020) and laboratory experiments (e.g., Leeman et al., 2018, 2016; Shreedharan et al., 2020) is that the critical stiffness criterion be met. In other words, the fault loading stiffness ($k$) cannot exceed the critical rate of frictional weakening with slip ($k_c$) defined as

$$k \leq k_c = \frac{\sigma_{eff}(b-a)}{D_c} \quad (7)$$

In the framework described by Equation 7, slow earthquakes naturally emerge when $k$ approaches $k_c$ (e.g., Liu & Rice, 2007; Leeman et al., 2016). This criterion can also be written in terms of a critical nucleation patch size, $h^*$ (Dieterich, 1992), wherein the stiffness $k$ is given by $k = \sim G/h^*$, where $G$ represents a shear modulus. In this context, a larger slip patch at nucleation (h*) leads to a lower stiffness, and hence a greater tendency for instability to arise. From Equation 7, one can observe that if the fault is velocity strengthening, that is, (a-b) is positive, then the critical stiffness criterion can never be met. Thus, in this framework, a velocity strengthening fault cannot nucleate an instability or rupture (Gu et al., 1984).

### 5.1. Scaling of RSF Parameters With Slip Rate

We observe that the RSF parameters (a-b) becomes more positive and $D_c$ increases with slip rate. This indicates that for a case where $k < k_c$ such that unstable slip may initiate, $k_c$ decreases as slip velocity grows (i.e., during the nucleation phase of an instability), thus bringing it closer to $k$ and energetically favoring slow rupture or stable sliding rather than an elastodynamic earthquake. This has been inferred from laboratory measurements (e.g., Ikari et al., 2013; Kaproth & Marone, 2013; Saffer & Wallace, 2015; Leeman et al., 2016, 2018) and demonstrated by recent numerical simulations by Im et al. (2020) who assume a fault with velocity dependent (a-b) and $D_c$ as we document here (Figure 6). Not only does this velocity-dependence favor slow slip, it increases the range of $k/k_c$ values where slow slip is favored (Im et al., 2020) and no longer necessitates extremely low effective normal stresses as is often required in numerical models of rupture to sustain slow slip (e.g., Liu & Rice, 2009; Shibazaki et al., 2019). Numerical models have successfully incorporated the velocity-dependence of frictional stability *(a-b)* by using a cut-off velocity (e.g., Rubin, 2008; Shibazaki & Shimamoto, 2007) where the fault exhibits velocity-weakening friction below the cut-off velocity and transitions to a velocity-strengthening friction above this value. In our experiments, this transitional velocity apparently coincides with the peak slip rates of the shallow SSEs documented at the northern Hikurangi margin (Figure 6c). However, this does not preclude the possibility that instabilities hosted by these lithologies far exceed this transitional velocity (Im et al., 2020).

### 5.2. Mechanisms Explaining the Velocity Dependence of the Critical Slip Distance, $D_c$

Because $D_c$ is a parameter that is difficult to directly estimate and may only be constrained via inversion, we illustrate the velocity dependence of $D_c$ directly by stacking multiple velocity steps with different initial velocities (Figures 7a and 7b). Naturally, this gives rise to questions surrounding the physical mechanisms that cause $D_c$ to increase with slip rate. We explore dilatant strengthening and broadening of the slip zone as a candidate mechanism for the velocity-dependence of apparent or effective $D_c$ (e.g., Marone et al., 1990; Marone et al., 2009; Samuelson et al., 2009, 2011), in part, because it has been suggested as a mechanism that could produce slow slip events (Segall et al., 2010). Dilatant strengthening is a mechanism where a rapid increase in fault zone dilation as slip rate initially increases causes a transient undrained decrease in local pore pressure, thus instantaneously increasing the local effective normal stress. As fault slip velocity increases, the fault zone dilates producing a local drop in pore pressure. This has been documented in lab studies as overprinting on the friction data by apparently increasing the $D_c$ or the distance over which the fault achieves a new steady-state friction (Samuelson et al., 2009, 2011).

Based on our data showing velocity-dependent $D_c$ in the 100% relative humidity (RH) experiments (Figure 7b) on the volcaniclastic facies and those by Mair and Marone (1999) on quartz gouge at room humidity, we suggest that dilatant strengthening may not be the primary, intrinsic control on the velocity-dependence of $D_c$. In the case of rough, planar (or saw-cut) faults, $D_c$ is usually defined as a microscopic asperity dimension (Marone, 1998). However, for our granular fault gouge with a finite volume and numerous shear fabrics (e.g., Kenigsberg et al., 2019), we recast $D_c$ as the width of a localized shear zone. Marone and Kilgore (1993) have previously suggested this interpretation of $D_c$ for fault gouge based on their observations of decreasing $D_c$ with increasing shear strain, as the shear fabrics become more well-developed and deformation is increasingly accommodated in shear-parallel boundary and Y-shear fabrics. Moreover, this is also consistent with our observation of the lack of a velocity dependence of $D_c$ in the case of velocity steps in the single-direct shear apparatus (Figure 6d and Figure S2 in Supporting Information S1), which forces localized slip as an experimental boundary condition.

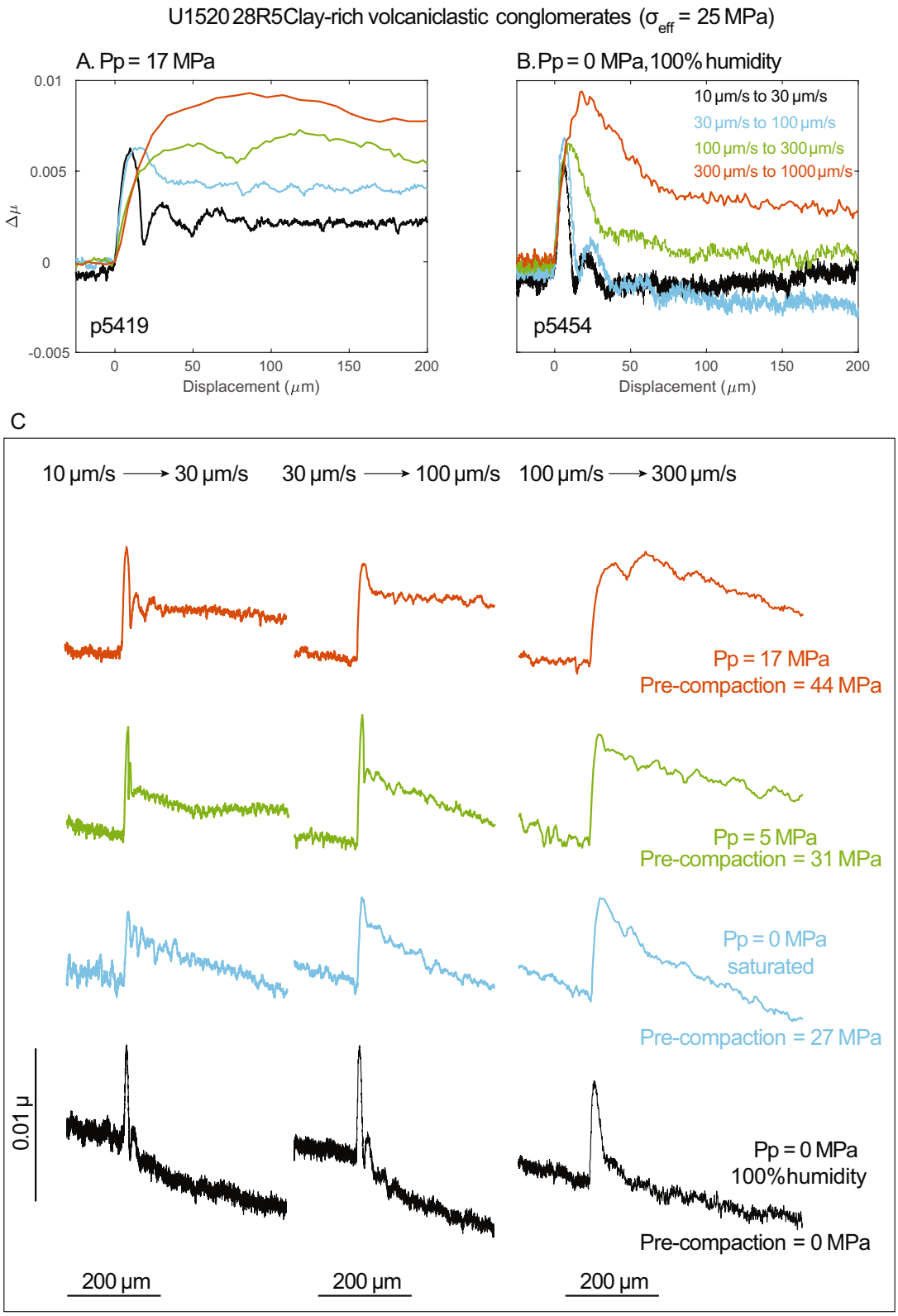


**Figure 7.**

We investigate dilatant strengthening as an additional possible mechanism by comparing velocity stepping experiments conducted in a saturated and pressurized fault to those on a fault in a 100% RH environment (Figures 7a and 7b). We document higher values of $D_c$ for higher sliding rates in both cases. However, while this increase is modest in the humid fault, that is, ~10–75 μm for a 100x increase in loading velocity, the $D_c$ increase is greater for the saturated fault (~40–250 μm for a 30× increase in loading velocity). As an additional validation exercise, we conduct velocity stepping experiments in four scenarios where the fault is pressurized to different degrees prior to shear at the same effective normal stress of 25 MPa (Figure 7c).

At higher $P_P$, the fault stabilizes and exhibits reduced slip weakening, lower values of the RSF parameter $b$ and modestly higher values of $D_c$ (Figure 7c and Figure S3 in Supporting Information S1). The dependence of rate-state frictional parameters on $P_P$ has previously been demonstrated in a limited number of studies (Bedford et al., 2021; Scuderi & Collettini, 2016; Xing et al., 2019). However, we note that due to the loading path (horizontal load is applied, then $P_c$, then $P_p$) in these experiments, there is also an unavoidable pre-compaction that scales with the amount of pore pressure applied. In this case, the different pre-compaction stresses would decrease the initial porosity and permeability of the fault, stiffen the fault and, by extension, influence dilatant strengthening to different degrees (Samuelson et al., 2009). Specifically, the experiment with largest pre-compaction stress (or lowest initial permeability) would experience the highest local pore pressure drop (and largest degree of dilatant strengthening) across a given velocity step. In other words, it is not possible to partition the stabilizing effects of $P_P$ and the pre-compaction on the RSF parameters. However, both stabilizing agents further support the possibility that dilatant strengthening is a non-trivial control on the velocity dependence of $D_c$.

Our results indicate the possibility that dilatant strengthening could play a significant role on the "apparent" values of RSF parameters via a competition between slip-dependent RSF parameters and time-dependent diffusion of fluids into the newly created pore spaces due to dilation. Moreover, our data are consistent with reports of dilatant strengthening on a range of gouge materials such as antigorite, olivine, quartz, chrysotile and serpentinite (French & Zhu, 2017; Xing et al., 2019) and direct observations of local pore-pressure drop during dynamic rupture in experimental faults (Brantut, 2020).

Thus, we suggest that velocity-dependent shear delocalization, and in turn, evolution of $D_c$, could be a significant factor in shallow SSE behavior, and future work incorporating careful measurements of layer thickness during experiments and associated microstructural analyses could more robustly validate/quantify this hypothesis.

### 5.3. Mineralogical Controls on Frictional Behavior

Significant lithological heterogeneities have been documented based on core sections recovered during IODP Expeditions 372/375 from Site U1520 (Barnes et al., 2020). Specifically, the dominant mineral types have been identified as carbonates and smectite-clays (Figure 2), occurring in the marls, chalk and volcaniclastic conglomerates (Figures S4–S7 in Supporting Information S1). This represents an interplay of strength and frictional stability that could control the rich suite of shallow slip behaviors documented at the northern Hikurangi margin. The carbonate-rich chalk lithology is characterized by high frictional strength, high healing rates and frictional velocity-dependence spanning velocity-neutral to strengthening behaviors (Figure 8). Additionally, carbonate-bearing faults also undergo pressure solution enhanced healing at hydrothermal conditions (Chen et al., 2015; Chen & Spiers, 2016) which is not fully captured in our experiments due to relatively short (maximum 3000 s) hold times and room temperature conditions. Thus, we anticipate that our healing rates represent a lower bound on the potential healing that carbonates could undergo. In contrast, the deeper (>850 mbsf) smectite-rich volcaniclastic conglomerates are frictionally weak, and are velocity strengthening at slip rates over 0.1 μm/s (Figure 8). This response indicates that the frictional behavior of the clay-fractions dominates the frictional response of volcaniclastic conglomerates. Our observations are consistent with numerous studies documenting that as little as 20% (by weight) of phyllosilicate-fraction can dominate the frictional behavior of mixed gouge (Giorgetti et al., 2015;

**Figure 7.** Evolution of the critical slip distance, $D_c$, with fault slip rate and pore pressure in experiments conducted on the clay-rich volcaniclastic conglomerates from sample U1520 28R5. (a) Overlay of four velocity steps in experiment with $P_P$ = 17 MPa shows that it takes more displacement for the friction to reach a post-step steady-state value for velocity steps at higher velocities. (b) Overlay of four velocity steps in experiment with 100% relative humidity (RH) shows that it takes more displacement for the friction to reach a post-step steady-state value for velocity steps at higher velocities, even with no pore fluids. (c) Matrix of different velocity steps at different hydration states shows the velocity dependence of $D_c$ and the 'evolution' effect for all values of $P_P$. However, this effect is more prominent for larger $P_P$ values likely due to dilatant strengthening.

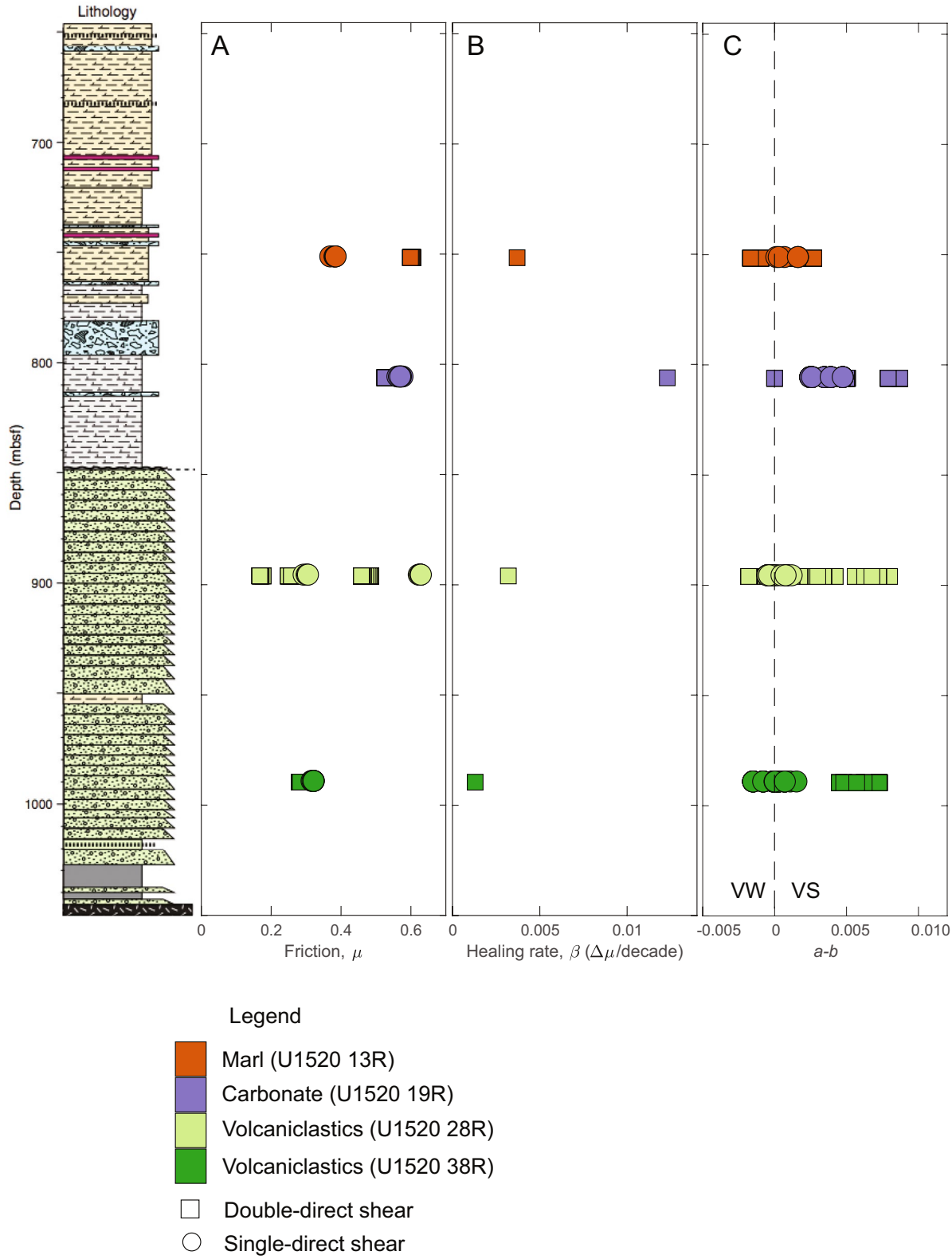


**Figure 8.** Variation of (a) coefficient of friction (b) healing rate and (c) frictional stability, (a-b) with depth at site U1520. Different colors represent different material/samples and the symbols represent double direct-shear (square) and single-direct shear (circle) apparatuses.

Ikari et al., 2007; Logan & Rauenzahn, 1987; Saffer & Marone, 2003). Finally, marls composed of ~35% phyllosilicates, 50% carbonates, and 15% quartz + feldspars are characterized by an intermediate frictional response between the chalk and volcaniclastic lithologies in the case of saturated faults whereas dry (or 100% RH) marls are frictionally strong.

Our results are broadly consistent with experiments previously performed by Boulton et al. (2019) and Rabinowitz et al. (2018) on samples from Leg 181 ODP Site 1124 in the Hikurangi Plateau which is ~500 km from the Hikurangi Trench. Rabinowitz et al. (2018) conducted friction experiments on late-Miocene clay-bearing nannofossil chalks (43% Calcite, 20% Phyllosilicates, 9% Quartz, 15% Feldspar) which are compositionally most similar to the marls in this study. Their experiments were conducted over a range of velocities (0.003–300 μm/s), effective stresses (1–26 MPa) and temperatures (25°C–110°C). They demonstrated a general velocity dependence of *(a-b)* similar to our results here (Figure 6c), decreasing frictional strength with increasing normal stress consistent with the dominance of phyllosilicates, and a general insensitivity to temperature (up to at least 110°C).

Experiments by Boulton et al. (2019) on mid-Paleocene to early Oligocene samples, representing a range of lithologies including nannofossil chalk, nannofossil-bearing zeolitic mudstone and mudstones bearing >50% clay minerals, were conducted over a range of velocities (0.3–100 μm/s) and temperatures (25°C–225°C). At room temperature, the weak clay-rich sediments exhibit velocity-neutral/weakening behavior consistent with our observations on the volcaniclastic conglomerates from Site U1520 albeit at different effective stresses. At higher temperatures, Boulton et al. (2019) documented a transition from rate-weakening to strengthening behavior in the clay-rich sediments. In contrast, the strong chalks are relatively stable at room temperature, as we document here in the 19R samples, and transition to strongly rate-weakening behavior at elevated temperatures (Boulton et al., 2019). Taken together, our observations and those of Boulton et al. (2019) and Rabinowitz et al. (2018) provide important constraints on the along-strike behavior of seismicity at the Hikurangi margin, particularly as these observations span a range of slip rates, temperatures, effective stresses, pore pressures and deformation apparatuses.

We integrate our experimental measurements of healing with geodetically derived constraints from stress drop and recurrence interval of SSEs at the Hikurangi margin and seismologically estimated stress drops for a global catalog of fast earthquakes (Figure 9). Specifically, we constrain healing for "ordinary"earthquakes using a global catalog of fast, elastodynamic seismicity with relatively well-resolved recurrence intervals (Kanamori & Allen, 1986), and estimate their stress drops from moment magnitudes using a circular crack model (Brune, 1970). These earthquakes represent a moment magnitude, $M_w$, range of 5.6–7.8 and recurrence times of the order of ~50–60,000 years (Kanamori & Allen, 1986). Based on fits to the log-linear relationship between the static stress drop and recurrence times for these earthquakes, we estimate an average healing rate of ~1.6 MPa/decade. Because these earthquakes represent a range of depths and hydrothermal conditions which could control healing rates (Carpenter et al., 2016), our calculations provide a qualitative estimate of healing rates which can be compared with SSEs. Our observations of the stress drop—recurrence time relationship for SSEs at the northern Hikurangi margin (Bartlow et al., 2014; Wallace & Beavan, 2010) low healing and small stress drops (~10 s of kPa) for the shallow SSEs in this region. This is consistent with the low static stress-drop model of SSE nucleation (Brodsky & Mori, 2007; Ide et al., 2007; Segall et al., 2010) and low inferred values of stress drops associated with the northern Hikurangi SSEs (Bartlow et al., 2014) and SSEs globally (Bürgmann, 2018).

Our experimental estimates of healing (and healing rates) in the chalk and volcaniclastic facies provide depth-dependent constraints on healing rates when extrapolated to hold times consistent with the recurrence duration of the quasi-periodic shallow SSEs at the northern Hikurangi margin. Specifically, we consider two end-member scenarios to estimate maximum and minimum stress healing rates (MPa/decade) for mixtures of the subducting sediments—a carbonate-rich fault and little/no pore-fluid overpressures representing the highest healing rates, and a smectite-rich fault with significant (locally undrained) overpressures representing the lowest healing rates at an effective stress of 25 MPa. The geodetically defined healing rate (0.1 MPa/decade) is intermediate between the high healing rates (~0.31 MPa/decade) of carbonate faults and the lower healing rates (~0.03 MPa/decade) of the volcaniclastic conglomerates. Broadly, our results indicate that mixing between the strong, brittle carbonates and the weak, viscous clay minerals could be an important two-phase mineralogical control on healing and shallow SSE nucleation at the northern Hikurangi margin, consistent with structural observations by Leah et al. (2020). Because the shallow portion of the northern Hikurangi margin is relatively cold (Antriasian

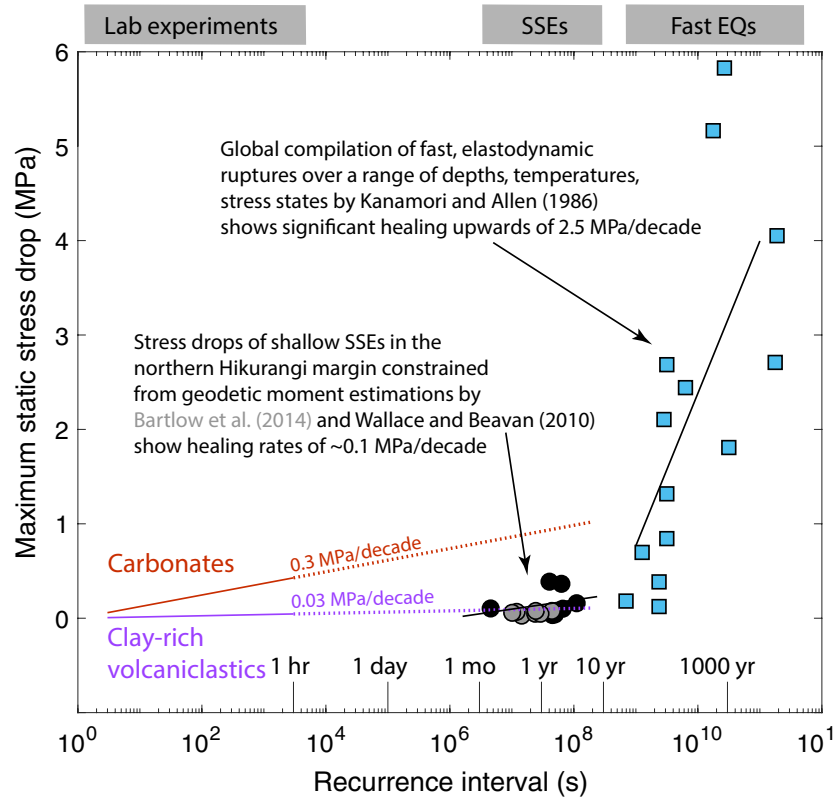


**Figure 9.** Compilation of fault healing from slide-hold-slide experiments in this study and earthquake stress drops for the northern Hikurangi slow earthquakes (Bartlow et al., 2014; Wallace & Beavan, 2010) and a global catalog of fast earthquakes (Kanamori & Allen, 1986) shows the remarkably low healing rates for the clay-rich volcaniclastic samples tested in this study and the shallow slow earthquakes at the northern Hikurangi margin.

et al., 2019; McCaffrey et al., 2008), we do not consider the role of temperature here, but it could be an additional control at depth, particularly downdip of the seismogenic zone.

### 5.4. Implications for Shallow SSEs at the Northern Hikurangi Margin

We present a conceptual model of subduction at the Hikurangi margin based on our observations of velocity-dependent friction and the strong mineralogical controls on frictional behavior (Figure 10). In this model, frictional (carbonates, seamounts) and geometric (seamounts) asperities on the downgoing plate are embedded in (or mix with) a viscous matrix of predominantly velocity-neutral, frictionally weak volcaniclastic conglomerates which exhibit low healing rates, indicating an inability to store elastic strain energy over long timescales. Shallow instabilities may nucleate in the strong carbonates with high healing rates at modestly elevated temperatures and/or stresses since carbonates have been seen to exhibit a transition from strengthening to velocity-weakening behavior at higher-than-room temperatures (~70°C; Boulton et al., 2019; Ikari et al., 2013; Kurzawski et al., 2016). However, a combination of intrinsically velocity-dependent friction (i.e., velocity-dependence of $a$-$b$ and $D_c$) and dilatant strengthening enhanced by potentially over-pressurized pore-fluids may arrest these instabilities, thus manifesting as shallow slow earthquakes. Shallow instabilities nucleating in the basaltic seamounts, depending on the degree of alteration experienced by the basalts (Cox, 1990; Ikari, Wilckens, & Saffer, 2020), could also propagate as SSEs. Further, numerical models of shallow SSEs incorporating a cut-off velocity (Shibazaki et al., 2019) or explicit velocity dependence of friction parameters (Im et al., 2020) have qualitatively reproduced the range of slip behaviors documented here. At seismogenic depths (>7–10 km), pressure-temperature conditions are conducive for carbonates to be significantly velocity weakening at all slip rates (e.g., Boulton et al., 2019; Ikari et al., 2013; Kurzawski et al., 2016), and thus, carbonates and/or basalts may nucleate instabilities that grow to be fast, dynamic earthquakes. In such cases, dynamic weakening could dominate in the shallower velocity-neutral/strengthening sediments thus preventing the ruptures from arresting (Aretusini et al., 2021; Di Toro et al., 2011;

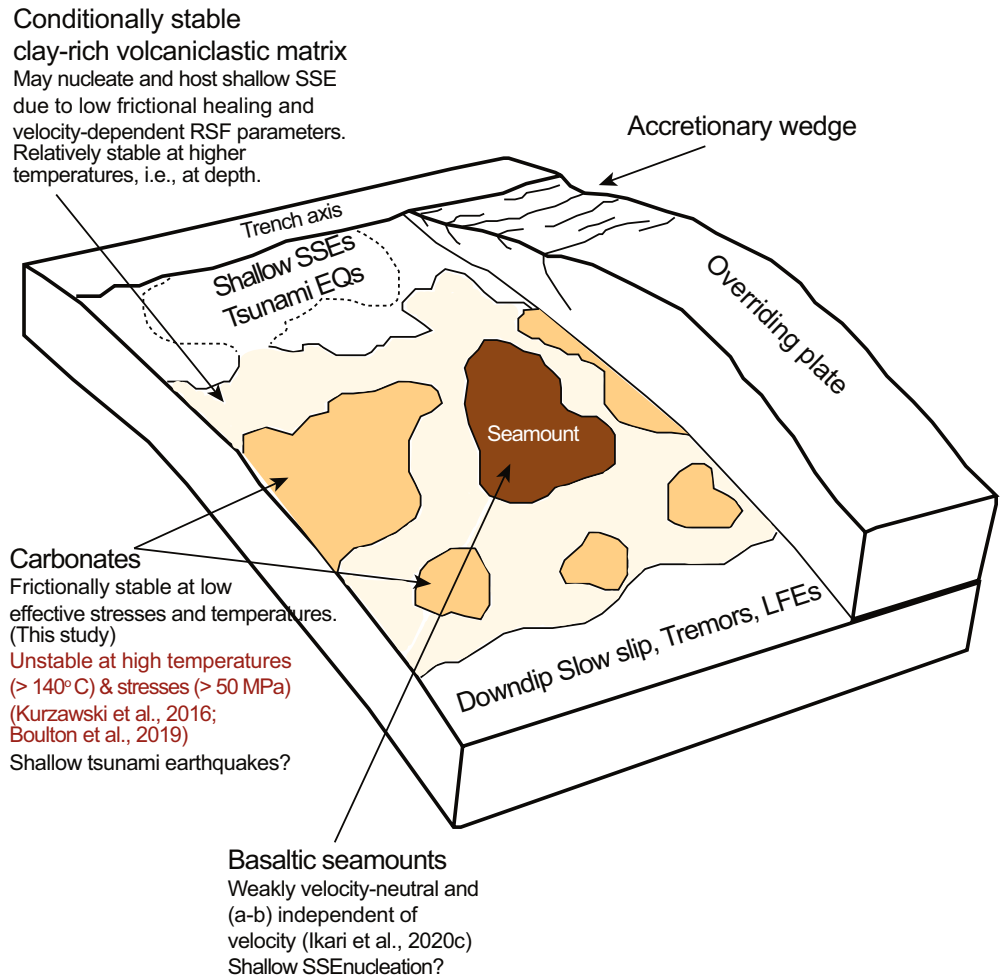


**Figure 10.** Illustrative cartoon showing summary of potential frictional and lithological controls on slow and fast earthquakes at the northern Hikurangi margin. In this view carbonate-rich patches and seamounts make up asperity patches in a velocity neutral/strengthening matrix of the abundant clay-rich volcaniclastic material at the plate interface. The volcaniclastic inputs to the plate interface at the northern Hikurangi margin are characterized by velocity-neutral friction at low slip rates transitioning to velocity strengthening friction at ~3 μm/s, velocity-dependent $D_c$ and exhibit extremely low (or zero) healing rates. The carbonate patches are nominally velocity strengthening at high slip rates, have velocity dependent $D_c$ and exhibit high healing rates at shallow depths consistent with the slow earthquakes. In this model, a carbonate asperity could nucleate a shallow instability whose slip rate is modulated by a combination of the inherent velocity dependence of friction ($a$-$b$ and $D_c$) and dilatant strengthening at high pore pressures which further enhances the velocity dependence of $D_c$ Modified from Lay et al. (2012).

Faulkner et al., 2011). Our conceptual model, motivated by experimental results indicating the strong role of the clay-rich volcaniclastic conglomerates and the second-order velocity-dependence of friction in modulating shallow slip behavior, provides insights into the mechanics of shallow SSEs at the northern Hikurangi margin.

## 6. Conclusions

We present a suite of friction experiments conducted on input material to the Hikurangi subduction margin recovered during IODP Expeditions 372/375. Specifically, we quantify the frictional strength, stability and healing behavior of the two dominant lithologies—carbonates and smectite-rich volcaniclastic conglomerates. We present velocity-dependent frictional parameters $(a\text{-}b)$ and $D_c$ as potentially important controls on shallow slow earthquake nucleation here. In particular, the transition in $(a\text{-}b)$ from velocity-weakening to strengthening behavior with increasing velocity could act as a rate-limiting agent, and the velocity-dependent increase in $D_c$ increases frictional stability by reducing the critical fault stiffness (or increasing the critical nucleation dimension) further favoring slower slip. Based on velocity-stepping experiments conducted on saturated and room-dry (humid) faults, we conclude that

the velocity-dependence of $D_c$ is likely due to a combination of dilatant strengthening and shear zone delocalization at higher fault slip rates. Finally, we compare experimentally determined frictional healing rates with geodetically inferred recurrence rates to demonstrate that the shallow slow earthquakes at the northern Hikurangi margin could be hosted by a mixture of strong, brittle carbonates and weak, viscous clay-rich sediments. Our results provide additional insights and constraints into the mechanics of shallow slow slip at the northern Hikurangi margin, and set the path for future investigations into the role of frictional heterogeneities on shallow SSEs.

## Data Availability Statement

Experimental data used in this study can be retrieved from https://doi.org/10.5281/zenodo.5199953.

**Acknowledgments**
We thank Steven Swavely for technical assistance with the biaxial experiments. This manuscript benefited from reviews by Carolyn Boulton and an anonymous reviewer. This study was supported by a US Science Support Program Schlanger Ocean Drilling Fellowship and a Post-Expedition Award to S. Shreedharan, European Research Council Advance Grant 835012 (TECTONIC), the US Department of Energy grants DESC0020512 and DE-EE0008763, and the US National Science Foundation grants EAR 1520760, EAR 1547441, and EAR 1763305 to C. Marone. This project has received funding from the European Research Council (ERC) under the European Union's Horizon 2020 research and innovation programme Grant No. 714430 to M. J. Ikari.

## References

Ando, R., Nakata, R., & Hori, T. (2010). A slip pulse model with fault heterogeneity for low-frequency earthquakes and tremor along plate interfaces. *Geophysical Research Letters*, *37*(10).
Antriasian, A., Harris, R. N., Trehu, A. M., Henrys, S. A., Phrampus, B. J., Lauer, R. et al. (2019). Thermal regime of the northern Hikurangi margin, New Zealand. *Geophysical Journal International*, *216*(2), 1177–1190.
Araki, E., Saffer, D. M., Kopf, A. J., Wallace, L. M., Kimura, T., Machida, Y. ., & Expedition, I. O. D. P. (2017). Recurring and triggered slow-slip events near the trench at the Nankai Trough subduction megathrust. *Science*, *356*(6343), 1157–1160.
Aretusini, S., Meneghini, F., Spagnuolo, E., Harbord, C. W., & Di Toro, G. (2021). Fluid pressurisation and earthquake propagation in the Hikurangi subduction zone. *Nature Communications*, *12*(1), 1–8.
Barker, D. H., Henrys, S., Caratori Tontini, F., Barnes, P. M., Bassett, D., Todd, E., & Wallace, L. (2018). Geophysical constraints on the relationship between seamount subduction, slow slip, and tremor at the north Hikurangi subduction zone, New Zealand. *Geophysical Research Letters*, *45*(23), 12–804.
Barnes, P. M., Wallace, L. M., Saffer, D. M., Bell, R. E., Underwood, M. B., Fagereng, A., et al. (2020). Slow slip source characterized by lithological and geometric heterogeneity. *Science Advances*, *6*(13), eaay3314.
Barnes, P. M., Wallace, L. M., Saffer, D. M., Pecher, I. A., Petronotis, K. E., LeVay, L. J., et al. (2019). Site U1520. In L. M. Wallace, D. M. Saffer, P. M. Barnes, I. A. Pecher, K. E. Petronotis, L. J. LeVay (Eds.), *Expedition 372/375 scientists, Hikurangi subduction margin coring, logging, and observatories. Proceedings of the International Ocean Discovery Program* (Vol. 372B/375). International Ocean Discovery Program. https://doi.org/10.14379/iodp.proc.372B375.105.2019
Bartlow, N. M., Wallace, L. M., Beavan, R. J., Bannister, S., & Segall, P. (2014). Time-dependent modeling of slow slip events and associated seismicity and tremor at the Hikurangi subduction zone, New Zealand. *Journal of Geophysical Research: Solid Earth*, *119*(1), 734–753.
Bassett, D., Sutherland, R., & Henrys, S. (2014). Slow wavespeeds and fluid overpressure in a region of shallow geodetic locking and slow slip, Hikurangi subduction margin, New Zealand. *Earth and Planetary Science Letters*, *389*, 1–13.
Bedford, J. D., Faulkner, D. R., Allen, M. J., & Hirose, T. (2021). The stabilizing effect of high pore-fluid pressure along subduction megathrust faults: Evidence from friction experiments on accretionary sediments from the Nankai Trough. *Earth and Planetary Science Letters*, *574*, 117161.
Beeler, N. M., Tullis, T. E., & Weeks, J. D. (1994). The roles of time and displacement in the evolution effect in rock friction. *Geophysical Research Letters*, *21*(18), 1987–1990.
Bell, R., Holden, C., Power, W., Wang, X., & Downes, G. (2014). Hikurangi margin tsunami earthquake generated by slow seismic rupture over a subducted seamount. *Earth and Planetary Science Letters*, *397*, 1–9.
Bell, R., Sutherland, R., Barker, D. H., Henrys, S., Bannister, S., Wallace, L., & Beavan, J. (2010). Seismic reflection character of the Hikurangi subduction interface, New Zealand, in the region of repeated Gisborne slow slip events. *Geophysical Journal International*, *180*(1), 34–48.
Boulton, C., Niemeijer, A. R., Hollis, C. J., Townend, J., Raven, M. D., Kulhanek, D. K., & Shepherd, C. L. (2019). Temperature-dependent frictional properties of heterogeneous Hikurangi Subduction Zone input sediments, ODP Site 1124. *Tectonophysics*, *757*, 123–139.
Brantut, N. (2020). Dilatancy-induced fluid pressure drop during dynamic rupture: Direct experimental evidence and consequences for earthquake dynamics. *Earth and Planetary Science Letters*, *538*, 116179.
Brodsky, E. E., & Mori, J. (2007). Creep events slip less than ordinary earthquakes. *Geophysical Research Letters*, *34*(16).
Brune, J. N. (1970). Tectonic stress and the spectra of seismic shear waves from earthquakes. *Journal of Geophysical Research*, *75*(26), 4997–5009.
Bürgmann, R. (2018). The geophysics, geology and mechanics of slow fault slip. *Earth and Planetary Science Letters*, *495*, 112–134.
Carpenter, B. M., Ikari, M. J., & Marone, C. (2016). Laboratory observations of time-dependent frictional strengthening and stress relaxation in natural and synthetic fault gouges. *Journal of Geophysical Research: Solid Earth*, *121*(2), 1183–1201.
Carpenter, B. M., Marone, C., & Saffer, D. M. (2011). Weakness of the San Andreas Fault revealed by samples from the active fault zone. *Nature Geoscience*, *4*(4), 251–254.
Carpenter, B. M., Saffer, D. M., & Marone, C. (2012). Frictional properties and sliding stability of the San Andreas fault from deep drill core. *Geology*, *40*(8), 759–762.
Chen, J., & Spiers, C. J. (2016). Rate and state frictional and healing behavior of carbonate fault gouge explained using microphysical model. *Journal of Geophysical Research: Solid Earth*, *121*(12), 8642–8665.
Chen, J., Verberne, B. A., & Spiers, C. J. (2015). Interseismic re-strengthening and stabilization of carbonate faults by "non-Dieterich" healing under hydrothermal conditions. *Earth and Planetary Science Letters*, *423*, 1–12.
Cox, S. J. D. (1990). Velocity-dependent friction in a large direct shear experiment on gabbro. *Geological Society, London, Special Publications*, *54*(1), 63–70.
Di Toro, G., Han, R., Hirose, T., De Paola, N., Nielsen, S., Mizoguchi, K. ., & Shimamoto, T. (2011). Fault lubrication during earthquakes. *Nature*, *471*(7339), 494–498.
Dieterich, J. H. (1972). Time-dependent friction in rocks. *Journal of Geophysical Research*, *77*(20), 3690–3697.
Dieterich, J. H. (1978). Time-dependent friction and the mechanics of stick-slip. In *Rock friction and earthquake prediction* (pp. 790–806). Birkhäuser. https://doi.org/10.1007/978-3-0348-7182-2_15

Dieterich, J. H. (1979). Modeling of rock friction: 1. Experimental results and constitutive equations. *Journal of Geophysical Research: Solid Earth*, *84*(B5), 2161–2168.
Dieterich, J. H. (1992). Earthquake nucleation on faults with rate-and state-dependent strength. *Tectonophysics*, *211*(1–4), 115–134.
Ellis, S., Fagereng, Å., Barker, D., Henrys, S., Saffer, D., Wallace, L., et al. (2015). Fluid budgets along the northern Hikurangi subduction margin, New Zealand: The effect of a subducting seamount on fluid pressure. *Geophysical Journal International*, *202*(1), 277–297.
Faulkner, D. R., Mitchell, T. M., Behnsen, J., Hirose, T., & Shimamoto, T. (2011). Stuck in the mud? Earthquake nucleation and propagation through accretionary forearcs. *Geophysical Research Letters*, *38*(18).
French, M. E., & Zhu, W. (2017). Slow fault propagation in serpentinite under conditions of high pore fluid pressure. *Earth and Planetary Science Letters*, *473*, 131–140.
Frye, K. M., & Marone, C. (2002). Effect of humidity on granular friction at room temperature. *Journal of Geophysical Research: Solid Earth*, *107*(B11). ETG-11.
Giorgetti, C., Carpenter, B. M., & Collettini, C. (2015). Frictional behavior of talc-calcite mixtures. *Journal of Geophysical Research: Solid Earth*, *120*(9), 6614–6633.
Gray, M., Bell, R. E., Morgan, J. V., Henrys, S., Barker, D. H., & IODP Expedition 372 and 375 science parties. (2019). Imaging the shallow subsurface structure of the North Hikurangi Subduction Zone, New Zealand, using 2-D full-waveform inversion. *Journal of Geophysical Research: Solid Earth*, *124*(8), 9049–9074.
Gu, J. C., Rice, J. R., Ruina, A. L., & Simon, T. T. (1984). Slip motion and stability of a single degree of freedom elastic system with rate and state dependent friction. *Journal of the Mechanics and Physics of Solids*, *32*(3), 167–196.
Ide, S., Beroza, G. C., Shelly, D. R., & Uchide, T. (2007). A scaling law for slow earthquakes. *Nature*, *447*(7140), 76–79.
Ikari, M. J., Carpenter, B. M., & Marone, C. (2016). A microphysical interpretation of rate-and state-dependent friction for fault gouge. *Geochemistry, Geophysics, Geosystems*, *17*(5), 1660–1677.
Ikari, M. J., Carpenter, B. M., Scuderi, M. M., Collettini, C., & Kopf, A. J. (2020). Frictional strengthening explored during non-steady state shearing: Implications for fault stability and slip event recurrence time. *Journal of Geophysical Research: Solid Earth*, *125*(10), e2020JB020015.
Ikari, M. J., Ito, Y., Ujiie, K., & Kopf, A. J. (2015). Spectrum of slip behaviour in Tohoku fault zone samples at plate tectonic slip rates. *Nature Geoscience*, *8*(11), 870–874.
Ikari, M. J., Marone, C., Saffer, D. M., & Kopf, A. J. (2013). Slip weakening as a mechanism for slow earthquakes. *Nature Geoscience*, *6*(6), 468–472.
Ikari, M. J., & Saffer, D. M. (2011). Comparison of frictional strength and velocity dependence between fault zones in the Nankai accretionary complex. *Geochemistry, Geophysics, Geosystems*, *12*(4).
Ikari, M. J., Saffer, D. M., & Marone, C. (2007). Effect of hydration state on the frictional properties of montmorillonite-based fault gouge. *Journal of Geophysical Research: Solid Earth*, *112*(B6).
Ikari, M. J., Saffer, D. M., & Marone, C. (2009). Frictional and hydrologic properties of clay-rich fault gouge. *Journal of Geophysical Research: Solid Earth*, *114*(B5).
Ikari, M. J., Wallace, L. M., Rabinowitz, H. S., Savage, H. M., Hamling, I. J., & Kopf, A. J. (2020). Observations of laboratory and natural slow slip events: Hikurangi subduction zone, New Zealand. *Geochemistry, Geophysics, Geosystems*, *21*(2), e2019GC008717.
Ikari, M. J., Wilckens, F. K., & Saffer, D. M. (2020). Implications of basement rock alteration in the Nankai Trough, Japan for subduction megathrust slip behavior. *Tectonophysics*, *774*, 228275.
Im, K., Saffer, D., Marone, C., & Avouac, J. P. (2020). Slip-rate-dependent friction as a universal mechanism for slow slip events. *Nature Geoscience*, *13*(10), 705–710.
Kanamori, H., & Allen, C. R. (1986). *Earthquake repeat time and average stress drop*.
Kaproth, B. M., & Marone, C. (2013). Slow earthquakes, preseismic velocity changes, and the origin of slow frictional stick-slip. *Science*, *341*(6151), 1229–1232.
Kaproth, B. M., & Marone, C. (2014). Evolution of elastic wave speed during shear-induced damage and healing within laboratory fault zones. *Journal of Geophysical Research: Solid Earth*, *119*(6), 4821–4840.
Kato, A., Obara, K., Igarashi, T., Tsuruoka, H., Nakagawa, S., & Hirata, N. (2012). Propagation of slow slip leading up to the 2011 Mw 9.0 Tohoku-Oki earthquake. *Science*, *335*(6069), 705–708.
Kenigsberg, A. R., Rivière, J., Marone, C., & Saffer, D. M. (2019). The effects of shear strain, fabric, and porosity evolution on elastic and mechanical properties of clay-rich fault gouge. *Journal of Geophysical Research: Solid Earth*, *124*(11), 10968–10982.
Kurzawski, R. M., Stipp, M., Niemeijer, A. R., Spiers, C. J., & Behrmann, J. H. (2016). Earthquake nucleation in weak subducted carbonates. *Nature Geoscience*, *9*(9), 717–722.
Lay, T., Kanamori, H., Ammon, C. J., Koper, K. D., Hutko, A. R., Ye, L., & Rushing, T. M. (2012). Depth-varying rupture properties of subduction zone megathrust faults. *Journal of Geophysical Research: Solid Earth*, *117*(B4).
Leah, H., Fagereng, Å., Meneghini, F., Morgan, J. K., Savage, H. M., Wang, M. ., & Ikari, M. J. (2020). Mixed brittle and viscous strain localization in pelagic sediments seaward of the Hikurangi Margin, New Zealand. *Tectonics*, *39*(8), e2019TC005965.
Leeman, J. R., Marone, C., & Saffer, D. M. (2018). Frictional mechanics of slow earthquakes. *Journal of Geophysical Research: Solid Earth*, *123*(9), 7931–7949.
Leeman, J. R., Saffer, D. M., Scuderi, M. M., & Marone, C. (2016). Laboratory observations of slow earthquakes and the spectrum of tectonic fault slip modes. *Nature Communications*, *7*(1), 1–6.
Liu, Y., & Rice, J. R. (2007). Spontaneous and triggered aseismic deformation transients in a subduction fault model. *Journal of Geophysical Research*, *112*(B9).
Liu, Y., & Rice, J. R. (2009). Slow slip predictions based on granite and gabbro friction data compared to GPS measurements in northern Cascadia. *Journal of Geophysical Research*, *114*(B9).
Logan, J. M., & Rauenzahn, K. A. (1987). Frictional dependence of gouge mixtures of quartz and montmorillonite on velocity, composition and fabric. *Tectonophysics*, *144*(1–3), 87–108.
Mair, K., & Marone, C. (1999). Friction of simulated fault gouge for a wide range of velocities and normal stresses. *Journal of Geophysical Research*, *104*(B12), 28899–28914.
Marone, C. (1998). Laboratory-derived friction laws and their application to seismic faulting. *Annual Review of Earth and Planetary Sciences*, *26*(1), 643–696.
Marone, C., Cocco, M., Richardson, E., & Tinti, E. (2009). The critical slip distance for seismic and aseismic fault zones of finite width. *International Geophysics*, *94*, 135–162.
Marone, C., & Kilgore, B. (1993). Scaling of the critical slip distance for seismic faulting with shear strain in fault zones. *Nature*, *362*(6421), 618–621.

Marone, C., Raleigh, C. B., & Scholz, C. H. (1990). Frictional behavior and constitutive modeling of simulated fault gouge. *Journal of Geophysical Research*, *95*(B5), 7007–7025.
McCaffrey, R., Wallace, L. M., & Beavan, J. (2008). Slow slip and frictional transition at low temperature at the Hikurangi subduction zone. *Nature Geoscience*, *1*(5), 316–320.
Meng, L., Huang, H., Bürgmann, R., Ampuero, J. P., & Strader, A. (2015). Dual megathrust slip behaviors of the 2014 Iquique earthquake sequence. *Earth and Planetary Science Letters*, *411*, 177–187.
Nakata, R., Ando, R., Hori, T., & Ide, S. (2011). Generaiktion mechanism of slow earthquakes: Numerical analysis based on a dynamic model with brittle-ductile mixed fault heterogeneity. *Journal of Geophysical Research*, *116*(B8).
Peng, Z., & Gomberg, J. (2010). An integrated perspective of the continuum between earthquakes and slow-slip phenomena. *Nature Geoscience*, *3*(9), 599–607.
Rabinowitz, H. S., Savage, H. M., Skarbek, R. M., Ikari, M. J., Carpenter, B. M., & Collettini, C. (2018). Frictional behavior of input sediments to the Hikurangi Trench, New Zealand. *Geochemistry, Geophysics, Geosystems*, *19*(9), 2973–2990.
Rubin, A. M. (2008). Episodic slow slip events and rate-and-state friction. *Journal of Geophysical Research*, *113*(B11).
Ruina, A. (1983). Slip instability and state variable friction laws. *Journal of Geophysical Research*, *88*(B12), 10359–10370.
Saffer, D. M., Frye, K. M., Marone, C., & Mair, K. (2001). Laboratory results indicating complex and potentially unstable frictional behavior of smectite clay. *Geophysical Research Letters*, *28*(12), 2297–2300.
Saffer, D. M., & Marone, C. (2003). Comparison of smectite-and illite-rich gouge frictional properties: Application to the updip limit of the seismogenic zone along subduction megathrusts. *Earth and Planetary Science Letters*, *215*(1–2), 219–235.
Saffer, D. M., & Wallace, L. M. (2015). The frictional, hydrologic, metamorphic and thermal habitat of shallow slow earthquakes. *Nature Geoscience*, *8*(8), 594–600.
Saito, T., Ujiie, K., Tsutsumi, A., Kameda, J., & Shibazaki, B. (2013). Geological and frictional aspects of very-low-frequency earthquakes in an accretionary prism. *Geophysical Research Letters*, *40*(4), 703–708.
Samuelson, J., Elsworth, D., & Marone, C. (2009). Shear-induced dilatancy of fluid-saturated faults: Experiment and theory. *Journal of Geophysical Research: Solid Earth*, *114*(B12).
Samuelson, J., Elsworth, D., & Marone, C. (2011). Influence of dilatancy on the frictional constitutive behavior of a saturated fault zone under a variety of drainage conditions. *Journal of Geophysical Research: Solid Earth*, *116*(B10).
Scholz, C. H. (2019). *The mechanics of earthquakes and faulting*. Cambridge university press.
Schwartz, S. Y., & Rokosky, J. M. (2007). Slow slip events and seismic tremor at circum-Pacific subduction zones. *Reviews of Geophysics*, *45*(3).
Scuderi, M. M., & Collettini, C. (2016). The role of fluid pressure in induced vs. triggered seismicity: Insights from rock deformation experiments on carbonates. *Scientific Reports*, *6*(1), 1–9.
Scuderi, M. M., Collettini, C., Viti, C., Tinti, E., & Marone, C. (2017). Evolution of shear fabric in granular fault gouge from stable sliding to stick slip and implications for fault slip mode. *Geology*, *45*(8), 731–734.
Segall, P., Rubin, A. M., Bradley, A. M., & Rice, J. R. (2010). Dilatant strengthening as a mechanism for slow slip events. *Journal of Geophysical Research: Solid Earth*, *115*(B12).
Shibazaki, B., & Shimamoto, T. (2007). Modelling of short-interval silent slip events in deeper subduction interfaces considering the frictional properties at the unstable—Stable transition regime. *Geophysical Journal International*, *171*(1), 191–205.
Shibazaki, B., Wallace, L. M., Kaneko, Y., Hamling, I., Ito, Y., & Matsuzawa, T. (2019). Three-dimensional modeling of spontaneous and triggered slow-slip events at the Hikurangi subduction zone, New Zealand. *Journal of Geophysical Research: Solid Earth*, *124*(12), 13250–13268.
Shreedharan, S., Bolton, D. C., Rivière, J., & Marone, C. (2020). Preseismic fault creep and elastic wave amplitude precursors scale with lab earthquake magnitude for the continuum of tectonic failure modes. *Geophysical Research Letters*, *47*(8), e2020GL086986.
Skarbek, R. M., Rempel, A. W., & Schmidt, D. A. (2012). Geologic heterogeneity can produce aseismic slip transients. *Geophysical Research Letters*, *39*(21).
Skarbek, R. M., & Savage, H. M. (2019). RSFit3000: A MATLAB GUI-based program for determining rate and state frictional parameters from experimental data. *Geosphere*, *15*(5), 1665–1676.
Tesei, T., Collettini, C., Barchi, M. R., Carpenter, B. M., & Di Stefano, G. (2014). Heterogeneous strength and fault zone complexity of carbonate-bearing thrusts with possible implications for seismicity. *Earth and Planetary Science Letters*, *408*, 307–318.
Tesei, T., Collettini, C., Carpenter, B. M., Viti, C., & Marone, C. (2012). Frictional strength and healing behavior of phyllosilicate-rich faults. *Journal of Geophysical Research: Solid Earth*, *117*(B9).
Todd, E. K., Schwartz, S. Y., Mochizuki, K., Wallace, L. M., Sheehan, A. F., Webb, S. C., et al. (2018). Earthquakes and tremor linked to seamount subduction during shallow slow slip at the Hikurangi margin, New Zealand. *Journal of Geophysical Research: Solid Earth*, *123*(8), 6769–6783.
Ujiie, K., Tanaka, H., Saito, T., Tsutsumi, A., Mori, J. J., Kameda, J., et al. (2013). Low coseismic shear stress on the Tohoku-Oki megathrust determined from laboratory experiments. *Science*, *342*(6163), 1211–1214.
Underwood, M. B. (2020). Data report: Reconnaissance of bulk sediment composition and clay mineral assemblages: Inputs to the Hikurangi subduction system. *Proceedings of the International Ocean Discovery Program*, 372.
Wallace, L. M. (2020). Slow slip events in New Zealand. *Annual Review of Earth and Planetary Sciences*, *48*, 175–203.
Wallace, L. M., Bartlow, N., Hamling, I., & Fry, B. (2014). Quake clamps down on slow slip. *Geophysical Research Letters*, *41*(24), 8840–8846.
Wallace, L. M., & Beavan, J. (2010). Diverse slow slip behavior at the Hikurangi subduction margin, New Zealand. *Journal of Geophysical Research: Solid Earth*, *115*(B12).
Wallace, L. M., Beavan, J., McCaffrey, R., & Darby, D. (2004). Subduction zone coupling and tectonic block rotations in the North Island, New Zealand. *Journal of Geophysical Research: Solid Earth*, *109*(B12).
Wallace, L. M., Kaneko, Y., Hreinsdóttir, S., Hamling, I., Peng, Z., Bartlow, N., et al. (2017). Large-scale dynamic triggering of shallow slow slip enhanced by overlying sedimentary wedge. *Nature Geoscience*, *10*(10), 765–770.
Wallace, L. M., Saffer, D. M., Barnes, P. M., Pecher, I. A., Petronotis, K. E., & LeVay, L. J. (2019). Hikurangi subduction margin coring, logging, and observatories. *Proceedings of the International Ocean Discovery Program*, 372.
Wallace, L. M., Webb, S. C., Ito, Y., Mochizuki, K., Hino, R., Henrys, S., et al. (2016). Slow slip near the trench at the Hikurangi subduction zone, New Zealand. *Science*, *352*(6286), 701–704.
Xing, T., Zhu, W., French, M., & Belzer, B. (2019). Stabilizing effect of high pore fluid pressure on slip behaviors of gouge-bearing faults. *Journal of Geophysical Research: Solid Earth*, *124*(9), 9526–9545.
Yasuhara, H., Marone, C., & Elsworth, D. (2005). Fault zone restrengthening and frictional healing: The role of pressure solution. *Journal of Geophysical Research: Solid Earth*, *110*(B6).